Hydrodynamic-Driven Stability Analysis of Morphological Patterns on Stalactites and Implications for Cave Paleoflow Reconstructions

Carlo Camporeale* and Luca Ridolfi

Department of Environment, Land, and Infrastructure Engineering, Politecnico di Torino, Corso Duca Abruzzi 24, 10129, Turin, Italy

(Received 7 January 2012; published 8 June 2012)

A novel hydrodynamic-driven stability analysis is presented for surface patterns on speleothems, i.e., secondary sedimentary cave deposits, by coupling fluid dynamics to the geochemistry of calcite precipitation or dissolution. Falling film theory provides the solution for the flow-field and depth perturbations, the latter being crucial to triggering patterns known as crenulations. In a wide range of Reynolds numbers, the model provides the dominant wavelengths and pattern celerities, in fair agreement with field data. The analysis of the phase velocity of ridges on speleothems has a potential as a proxy of past film flow rates, thus suggesting a new support for paleoclimate analyses.

DOI: 10.1103/PhysRevLett.108.238501 PACS numbers: 92.30.Xy, 47.20.Gv, 47.54.−r, 91.80.Wx

From time immemorial, karst speleothems, such as stalactites, stalagmites, draperies, flowstones, and helictites [1], have attracted the curiosity of most—scientists and common people alike—intrigued by the formidable variety of beautiful patterns, their ubiquity in caves, and the long time scales involved (10^3–10^5 yr). One of the most striking features of speleothems is the occurrence of morphological instabilities on the calcite surface at the contact with water. Speleothems in fact develop surface patterns over a wide range of Reynolds numbers, $R = \tilde{u}_f \tilde{D}/\nu$ ($\tilde{u}_f$ being the water surface velocity, $\tilde{D}$ the film depth, ν the kinematic viscosity, and the tilde a reference to dimensional quantities). The most recognized features are called *crenulations*, i.e., ripplelike structures with a subcentimetric wavelength, $\tilde{L}$, that develop at $R = O(10^{-2})$ during the deposition of $CaCO_3$ on stalactites from a supersaturated flow [Figs. 1(a) and 1(b)]. Other dunelike ridges can also arise on laminated deposits on the floor or walls of caves—i.e., flowstones—under turbulent sheet flows and perform larger length scales ($\tilde{L} \sim 10$ cm), but crenulations generated in laminar conditions (at $10^{-1} < R < 10$) and superimposed on flowstones are not unlikely to occur [Figs. 1(c) and 1(d)]. However, the wavelength of all crenulations is very similar, regardless of the Reynolds numbers. In the last decade, the analysis of isotope ratios, combined with high-resolution U^{230}-Th dating techniques, has popularized speleothems even in paleoclimatology [2], where the task is to reconstruct past temperatures, the CO_2 sources, and (through climate modeling) paleohydrology and paleorainfalls [3]. However, a morphological proxy of paleoflows in the cave is still missing.

This study addresses three major questions: Why do falling films generate crenulations on speleothems? Why do crenulations exhibit almost constant wavelengths, independently of hydrochemical conditions? Is there a potential for a paleoflow reconstruction based on hydrodynamic-oriented theory that may complement chemical analyses? Although calcite precipitation or dissolution geochemistry is nowadays well-understood [4], and despite the existence of a physical explanation of the universal laws of stalactites [5], to date, the mathematical problem of the morphological instability of speleothems remains unsolved. Indeed, a recent attempt to develop a linear stability analysis with a simplified depth-averaged model failed the prediction of the crenulation formation [6]. This failure is related to the subtle role played by the hydrodynamics of the thin water film which interacts with the surface, carries the solutes by convection and diffusion, and is the environment of the chemical reactions. In the following, crenulation instability is explained by combining a thorough description of geochemistry to a refined free-surface Orr-Sommerfeld-like model, under laminar conditions ($10^{-3} < R < 10$). Capillary and inertial effects will also be included.

Dynamics of calcareous speleothems involve four phases [2]: (i) soil activity and limestone dissolution of epikarst (the aquifer between the cave and the topsoil) enhance the content of dissolved CO_2 and Ca^{2+} in the groundwater; (ii) at the contact of the film with the cave's atmosphere—which typically has a lower CO_2 partial pressure, p_c, than epikarst—a quick degassing makes the solution supersaturated with respect to calcite and precipitation occurs on stalactites and stalagmites; (iii) water then flows on the walls and floor of the cave, where precipitation and calcium depletion continue up to its saturation concentration, c_s; and (iv) local changes in the external factors, e.g., temperature (T) or p_c, can modify c_s and trigger new precipitation or dissolution processes. Crenulations usually appear on stalactites in phases (ii)–(iii) and over flowstones in phase (iv).

According to the scheme of Fig. 1(f), the analysis is applied to a laminar flow that is bounded by the free surface (FS), $h(x, t)$, and the precipitation-dissolution calcite interface (PDI), $\eta(x, t)$, that is assumed to be locally flat in the unperturbed state. We will neglect 3D effects, but they may be readily englobed in the present theory. Following Short *et al.* [7], a separation of time scales

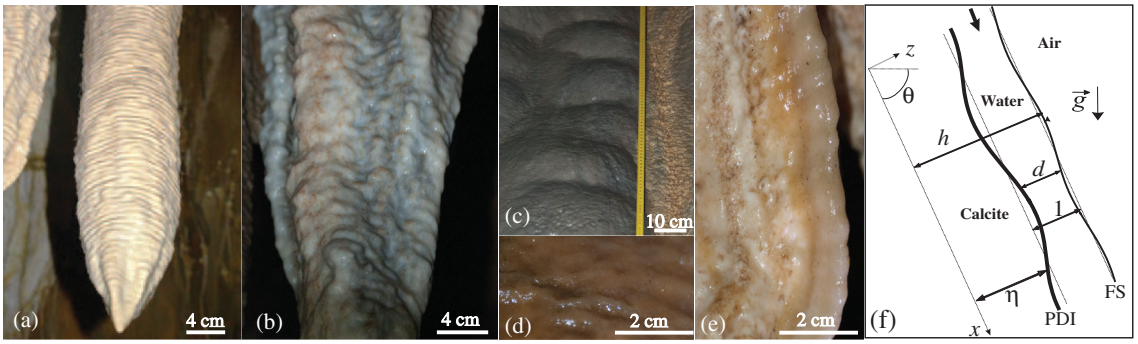

FIG. 1 (color). (a) Two-dimensional and (b) three-dimensional crenulations on stalactites. (c) Coexistence of ripple- and dunelike instabilities on flowstones. Crenulations on (d) flowstones and (e) draperies. Picture (a) was taken in Lehman Caves, Utah [14]. Pictures (b)–(e) are from Bossea Cave, Italy, where $\mathcal{C} \sim 190$ ppm, $T = 9\,^{\circ}\mathrm{C}$, and $p_c = 10^3$ ppm. (f) Sketch of the physical problem in dimensionless scales (in this Letter, we assume $\theta = \pi/2$).

between the calcite and hydrodynamics justifies the quasisteady approximation. The variables are made dimensionless using the length and velocity scales of Nusselt's velocity profile: $\tilde{D} = \Gamma^{-1}\nu^{2/3}R^{1/3}$ and $\tilde{u}_f = \Gamma(\nu R^2)^{1/3}$ (where $\Gamma = [g\sin(\theta)/2]^{1/3}$, g is the gravity acceleration, and θ is the tilting; see Fig. 1(f)). The dynamics of the ternary system H_2O-CO_2-$CaCO_3$ involve three concentrations, $\{\tilde{c}_1, \tilde{c}_2, \tilde{c}_3\} \equiv \{[Ca^{2+}], [CO_2], [HCO_3^-]\}$. If the incoming calcium concentration, $\tilde{c}_1|_{x=0} \equiv \mathcal{C}$, is used to provide a dimensionless representation of $\tilde{c}_1$ and $\tilde{c}_3$ and $\tilde{c}_2$ is scaled with its equilibrium concentration at the free surface, $\mathcal{H}p_c$ ($\mathcal{H}$ is the Henry's law constant), the steady-state vorticity and mass transport equations for 2D incompressible flows [8] read

$$(R\hat{\boldsymbol{\nabla}}\psi \cdot \boldsymbol{\nabla}^3 + \nabla^4)\psi = 0, \tag{1}$$

$$(P_i\hat{\boldsymbol{\nabla}}\psi \cdot \boldsymbol{\nabla} + \nabla^2)c_i + r_i = 0, \tag{2}$$

respectively, where $\boldsymbol{\nabla} = \{\partial_x, \partial_z\}$, $\hat{\boldsymbol{\nabla}} = \{-\partial_z, \partial_x\}$, $\psi(x, z)$ is the stream function, $P_i = \tilde{D}\tilde{u}_f/\mathcal{D}_i$ is the Péclet number, $\mathcal{D}_i$ is the diffusion coefficient of $\tilde{c}_i$, $r_1 = 0$, $r_2 = k_1c_2 - k_2c_3$, $r_3 = -r_2$, and the coefficients k_i are functions of temperature, pH, $\mathcal{C}$, $\mathcal{D}_i$, and $\tilde{D}$ [9]. The R-dependent term in (1) accounts for the inertial effects.

The PDI evolution is driven by three *rate-limited* reactions involving calcite, carbon dioxide, calcium, and carbonate ions [4], from which Plummer, Wigley, and Parkhurst [10] derived the so-called PWP equation for the calcite flux, $\tilde{f}$ [mol/m^2 s], at the PDI. It has been justified experimentally and reads

$$\tilde{f} = -\kappa_1(H^+) - \kappa_2(H_2CO_3^*) - \kappa_3 + \kappa_4(Ca^{2+}) \times (HCO_3^-), \tag{3}$$

with $(H_2CO_3^*) = (CO_2) + (H_2CO_3^0)$. The round brackets in (3) refer to activities, according to the Debye-Hückel theory, $(x) = \gamma_x \times [x]$, where γ_x is the activity coefficient that depends on the ionic strength I of the solution [11]. In the range $6 < p\mathrm{H} < 8$, the electroneutrality condition provides $I \sim 3\mathcal{C}$ [4]. The PWP equation is crucial to deriving the dispersion relation of the morphodynamic instability, but we first need to eliminate some chemical variables. To this aim, we use (i) the electroneutrality condition, (ii) the ionic product of water, (iii) the solubility product of calcite, and (iv) two *non-rate-limited* reactions involving $[H_2CO_3^0]$, $[CO_3^{2-}]$, and $\tilde{c}_3$ [4]. From (i)–(iv), one obtains $c_3 = a_1c_1 + a_2$ and $[H^+] = a_3c_1^2 \sim a_3\mathcal{C}^2$; i.e., pH is taken here as space-independent, whereas the dimensionless form of (3) becomes $f = \rho_0 + \rho_1c_1 + \rho_2c_2 + \rho_3c_1^2$ [9]. The problem is completed by suitable kinematic, dynamic, no-slip, and flux conditions written at the boundaries of the PDI and the FS,

$$f - \eta_{,t} = f + \chi c_{1,z} = c_{2,z} = \psi_{,x} = \psi_{,z} = 0, \text{ PDI}; \tag{4}$$

$$c_{1,z} = c_2 - 1 = \mathbf{n} \cdot \hat{\boldsymbol{\nabla}}\psi = \mathbf{n} \cdot \boldsymbol{\sigma} \cdot \boldsymbol{\tau} = \mathbf{n} \cdot \boldsymbol{\sigma} \cdot \mathbf{n} + \frac{R\mathcal{K}}{W} = 0, \text{ FS}, \tag{5}$$

where t is time, the comma in the subscript refers to partial derivatives, $\chi = \varrho\mathcal{C}/P_1$ (ϱ is the molar mass-to-density ratio of calcite), $\mathbf{n}$ and $\boldsymbol{\tau}$ are the unit normal and tangential vectors to FS, $\boldsymbol{\sigma}$ is the Newtonian stress tensor, $W = R(\Gamma^3/g)/l_c^2$ is the Weber number, l_c is the capillary length, and $\mathcal{K} = [(\mathbf{1} - \mathbf{n}{:}\mathbf{n}) \cdot \boldsymbol{\nabla}] \cdot \mathbf{n}/2$ is the FS curvature. The kinematic evolution equation [i.e., the first equality in Eq. (4)] plays the same role as the Exner and Stefan conditions in other morphodynamic problems [12,13].

Let us take advantage of Prandtl's mapping $z = \zeta d + \eta$, where $d = h - \eta$, so that the PDI is mapped to $\zeta = 0$ and the FS to $\zeta = 1$. We now perturb the generic quantity y appearing in (1), (2), (4), and (5) according to the ansatz $y = Y + \hat{y}e^{\lambda t + i\alpha x}$ ($|\hat{y}| \ll |Y|$, $i = \sqrt{-1}$). After linearizing around the unperturbed state (capital quantities), the zero order reads

$$\Psi' = 2\zeta - \zeta^2, \quad C_1 \sim 1, \quad C_2 \sim 1 + \omega(\zeta^2 - 1)k_1, \tag{6}$$

$$F = \frac{\rho_2}{2}(2 - k_1\omega) + \rho_0 + \rho_1 + \rho_3, \tag{7}$$

where the prime refers to $d/d\zeta$ and $\omega = [k_2(a_1 + a_2)/k_1] - 1$. The left-hand side of (6) is the Poiseuille law, and nonparallel effects in (6) and (7) have been neglected at the scale of $2\pi/\alpha$. At the first order, the hydrodynamic equations provide the steady-state open-channel version of the Orr-Sommerfeld problem, which is well-known in hydrodynamic stability theory. At $R \ll 1$, according to lubrication theory, the Orr-Sommerfeld equation reduces to the biharmonic equation; thus, exact solutions of $\hat{d}$ and $\hat{\psi}$ are easily achievable. Otherwise, the solutions can be written in terms of the Frobenius series (further details are in the Supplemental Material). Finally, the first-order mass transport equations read

$$\hat{c}_i'' - [\alpha_i + i\alpha P_i(2\zeta - \zeta^2)]\hat{c}_i = \hat{r}_i(\zeta), \tag{8}$$

$$\chi\hat{c}_1' + \hat{d}F + \hat{f} = \hat{c}_2' = 0, \text{ PDI}; \quad \hat{c}_1' = \hat{c}_2 = 0, \text{ FS}, \tag{9}$$

where $\alpha_i = \{\alpha^2, \alpha^2 - k_1\}$ and $\hat{r}_i = \{0, \hat{r}_{\mathcal{F}}(\hat{c}_1, \hat{\psi}) + \hat{f}\hat{r}_{\mathcal{G}}(\hat{c}_1)\}$ [9]. According to the structure of $\hat{r}_2$, we impose $\hat{c}_2 = \mathcal{F}(\zeta) + \hat{f}\mathcal{G}(\zeta)$, thus obtaining $\hat{c}_1(\zeta)$ and $\hat{c}_2(\zeta)$ from (8) and (9) in terms of the Frobenius series at $P_2 < 10^3$ and by a Chebyshev collocation method at $P_2 > 10^3$. An example of a solution of the (complex) functions $\{\hat{\psi}, \hat{c}_1, \hat{c}_2\}$ is reported in Fig. 2(a). Notice the large variations of these functions with respect to ζ, which precludes any simplified depth-averaged approach.

By combining (9) with the first-order term of the PWP equation ($\lambda = \hat{f}$), after some algebra, we obtain the dispersion relation

$$\lambda = \frac{F\hat{d}(\rho_1 + 2\rho_3)\mathcal{I}(0) - \rho_2\chi\mathcal{F}(0)}{\chi[\rho_2\mathcal{G}(0) - 1] - \mathcal{I}(0)(\rho_1 + 2\rho_3)}, \tag{10}$$

where the function $\mathcal{I}(\zeta)$ is a solution of (8) for $i = 1$, after imposing $\mathcal{I}'(1) - 1 = \mathcal{I}'(0) = 0$. We recall that $\mathrm{Re}(\lambda)$ is the growth rate and $c \equiv -\mathrm{Im}(\lambda)/\alpha$ is the phase velocity of perturbations. Accordingly, unstable [stable] conditions correspond to $\mathrm{Re}(\lambda) > 0$ [$\mathrm{Re}(\lambda) < 0$] and downstream [upstream] migration of individual ripples corresponds to $c > 0$ [$c < 0$].

Figure 2(b) shows the concentration field of an unstable case (contour plots) and the related calcite flux perturbation (dashed curve). The calcium distribution is distorted downstream by the Poiseuille flow and high (low) levels of concentrations of solutes are localized on the ridges (troughs). This is combined with a slight phase lead with respect to the bed, thus inducing an upstream-migrating instability of the PDI perturbation. We note incidentally that the role of the free-surface perturbation $\hat{d}$ is crucial in the above scenario. In fact, if $\hat{d}$ is forced to be null (that is, if FS is parallel to PDI), it can be shown that $\hat{c}_1 \sim 0$ and the calcite flux perturbation is therefore dramatically reduced. The time scale of the pattern growth, $\tilde{D}/\tilde{u}_f\mathrm{Re}(\lambda)$, in fact changes from $O(1)$ to $O(10^3)$ years.

By exploiting (10), we are able to find the wave number, α_m, which maximizes the growth rate of the perturbations, i.e., the most unstable one, while spanning different values of all the parameters, provided that a condition of net precipitation ($F > 0$) holds. This analysis is shown in Fig. 3, where the selected dimensionless wavelength is shown as a function of the Reynolds number, for different hydrochemical conditions. Despite a wide variation in the parameters, the behavior of the selected wavelength is sensitive to the Reynolds number but almost independent of changes in the chemical factors ($\mathcal{C}$ and p_c) and only weakly sensitive to temperature. In terms of a power law,

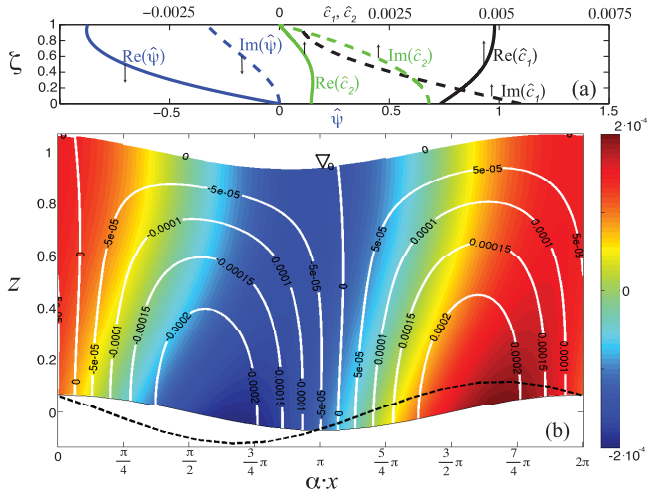

FIG. 2 (color). (a) Solution of Eqs. (8) and (9). (b) Spatial distributions of $\hat{c}_1$ (color scale) and $\hat{c}_2$ (white contour lines) in the physical domain; the dashed line shows the perturbed calcite flux magnified by a factor of 10^9. ($R = 0.05$, $\alpha = 0.044$, $\mathcal{C} = 300$ ppm, $p_c = 350$ ppm, and $T = 15\,^\circ$C.)

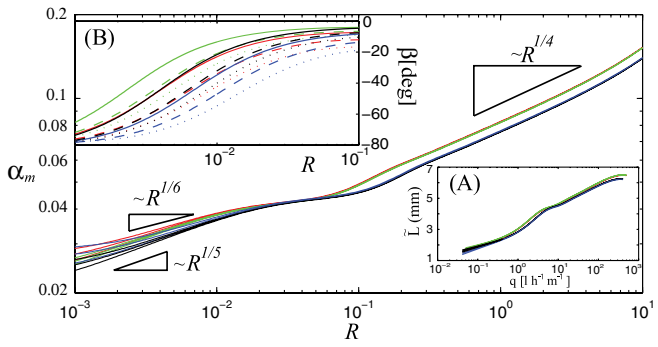

FIG. 3 (color online). The most unstable wave number in dimensionless (main figure) and dimensional (inset A) variables and the slope factor (inset B; see the text). Different combinations of (T [°C], p_c [ppm]) are reported in green (8, 350), blue (15, 350), red (8, 1000), and black (15, 1000) (in grayscale, from light gray to black). $\mathcal{C}$ values are in ppm: solid line, 100; dashed line, 250; dotted line, 500.

$\alpha_m \sim R^n$, two regimes can be distinguished: for $R < 0.1$, $n = 1/6$–$1/5$, depending on the parametric conditions; for $R > 0.1$, $n = 1/4$. Recalling that $\tilde{D} \sim R^{1/3}$, the dimensional wavelength turns out to be $\tilde{L} = 2\pi\tilde{h}/\alpha_m \sim R^p$, with $p = 0.08$–0.16. In dimensional terms, the ultimate R dependence is thus dramatically depleted. This aspect is shown by Fig. 3, inset A, which shows the dimensional wavelength of the selected patterns as confined in a very limited interval (0.2–0.7 cm), despite the five-order magnitude variation in the water unit discharge, $q = \tilde{D}\tilde{u}_f$.

This result is consistent with what is found in nature. Experimental observations confirm that crenulations tend to exhibit almost constant wavelengths, regardless of the boundary conditions (either physical or chemical), a finding that has remained for the most part unexplained so far. Here, we show that these dynamics are driven by hydrodynamical processes and that the typical length scales are determined by the physics of falling films. For instance, capillary effects appear to play a crucial role in wavelength selection. With a gradual decrease in the water surface tension (i.e., increase in W), the constancy of the wavelength is broken and a dramatic increase in $\tilde{L}$ can be observed (up to tenfold). Hence, any surfactant in the groundwater (e.g., from insecticides) is expected to induce some changes in the patterns. This theory is consistent with our observations from Bossea Cave, as evidenced by the size of the crenulations shown in Fig. 1. A further important result is that these patterns invariably migrate upstream ($c < 0$) in all our considered cases, with velocities from mm/yr to cm/yr, a novel finding that further enforces the similarity between crenulations and icicles.

We now analyze whether the above theory can provide the basis for a method that infers paleoflows on stalactites from an analysis of crenulation patterns. The above results suggest that the use of $\tilde{L}$ is not a good candidate for a successful methodology because of its small R dependence. Therefore, we consider the quantity $\beta = \tan^{-1}(c/F)$, which we name *slope factor*. It is straightforward to recognize that β is exactly the angle between any constant-phase point of the wavelet, moving outward during the deposition process, and the z axis. The slope factor is reported in the "stalactite" range ($10^{-3} < R < 10^{-1}$) in Fig. 3, inset B. This quantity appears to be highly sensitive to the flow conditions, β varying from $-90°$ to $-10°$ degrees (the negative sign is strictly related to the already mentioned upstream migration). Accordingly, Fig. 4 reports a preliminary experimental validation through the visual inspection of the slope factor imprinted in two different points of a stalactite specimen of Bossea Cave. It is worth noticing that wavelength evaluation is a quite hard task in this case, since the wavelet amplitude is weak. Nevertheless, the slope factor is easily identifiable and is negative for both of the points shown in Fig. 4, in agreement with the theory developed in this Letter. Furthermore, we are able to test the accuracy of the flow-rate assessment. From an estimation of the past cross sections corresponding to two marked points at different times, and assuming no changes in the total flow rate over time, we found that the Reynolds number ratio of the two cross sections is $R_a/R_b = \phi_b/\phi_a = 1.36$, where the subscripts indicate the points marked in Figs. 4(a) and 4(b) and ϕ refers to the diameter of the related cross section. Considering instead the values of β determined from Fig. 4, our theory gives $R_a = 0.0041$ and $R_b = 0.0029$, with a ratio equal to 1.41 and a satisfactory error of 3%.

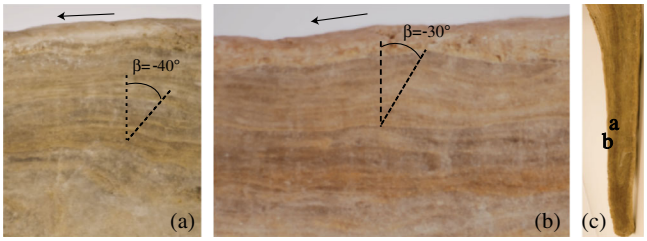

FIG. 4 (color online). Analysis of the slope factor on a stalactite from Bossea Cave ($\mathcal{C} \sim 190$ ppm, $T = 9\,°\mathrm{C}$, and $p_c = 10^3$ ppm). Panels (a) and (b) are close-ups of the marked points of the longitudinal section of the stalactite reported in panel (c). The arrows refer to the water flow direction.

Theoretical models have already shown that stalactites exhibit shapes that are overall universal [5]. By coupling hydrodynamical and chemical processes, the approach presented here explains the universality of the fine-grain structure of surface patterns, as well, in good agreement with cave data. Hydrodynamic processes play a crucial role in determining the wavelength selection of crenulations, thus providing another example of a free-boundary value problem involving a *morphodynamic* instability driven by a free surface, similar to the cases of sand dunes, ice ripples, and icicles [12,13]. The slope factor imprinted by paleoflows on crenulation records is a promising tool in paleoclimatology, particularly in continental regions, where the lack of ice and marine records calls for an improvement and extension of paleoclimatic methods [2,3]. An expeditious analysis based on paleocrenulation geometry might direct the location of the cores sampled for geochemical analyses.

We wish to acknowledge Professor B. Vigna for his support and assistance in Bossea Cave.

*carlo.camporeale@polito.it

[1] P. Meakin and B. Jamtveit, Proc. R. Soc. A **466**, 659 (2010).
[2] I. Fairchild, C. Smith, A. Baker, L. Fuller, C. Spotl, D. Mattey, and F. McDermott, Earth-Sci. Rev. **75**, 105 (2006).
[3] D. Genty, D. Blamart, R. Ouahdi, M. Gilmour, A. Baker, J. Jouzel, and S. Van-Exter, Nature (London) **421**, 833 (2003).

[4] G. Kaufmann and W. Dreybrodt, Geochim. Cosmochim. Acta **71**, 1398 (2007).
[5] M. Short, J. Baygents, J. Beck, D. Stone, R. Toomey, and R. Goldstein, Phys. Rev. Lett. **94**, 207 (2005).
[6] P. Y. Chan and N. Goldenfeld, Phys. Rev. E **76**, 046104 (2007).
[7] M. Short, J. Baygents, and R. Goldstein, Phys. Fluids **17**, 083101 (2005).
[8] G. Batchelor, *An Introduction to Fluid Dynamics* (Cambridge University Press, Cambridge, England, 1967).
[9] See Supplemental Material at http://link.aps.org/supplemental/10.1103/PhysRevLett.108.238501 for relationships for k_i, γ_i, a_i, ρ_i, $\hat{r}_{\mathcal{F}}$, and $\hat{r}_{\mathcal{G}}$ and for a derivation of Eqs. (1)–(5).
[10] L. Plummer, T. Wigley, and D. Parkhurst, Am. J. Sci. **278**, 179 (1978).
[11] W. Dreybrodt, *Processes in Karst Systems* (Springer, Berlin, 1988).
[12] C. Camporeale and L. Ridolfi, Phys. Fluids **23**, 104102 (2011).
[13] C. Camporeale and L. Ridolfi, J. Fluid Mech. **694**, 225 (2012).
[14] http://greatbasin.areaparks.com